Investigation of dust properties of the proto-planetary nebula IRAS 18276−1431

K. Murakawa[1], H. Izumiura[2], R. D. Oudmaijer[1], and L. T. Maud[1]

[1]*School of Physics and Astronomy, EC Stoner Building, University of Leeds, Leeds LS2 9JT*
[2]*Okayama Astrophysical Observatory, 3037-5 Honjo, Kamogata, Asakuchi, Okayama, 719-0232 Japan*

ABSTRACT

We investigate the circumstellar dust properties of the oxygen-rich bipolar proto-planetary nebula IRAS 18276–1431 by means of two-dimensional radiative transfer simulations of the circumstellar dust shell. The model geometry is assumed to have a torus and an envelope which consists of a pair of bipolar lobes and a spherical AGB shell. The parameters of the dust and the dust shell are constrained by comparing the spectral energy distribution (SED) and near-infrared intensity and polarisation data with the models. The polarisation in the envelope reaches 50 – 60 % and is nearly constant in the H and K_S bands in the observations. This weak wavelength dependence of the polarisation can be reproduced with a grain size distribution function for the torus: $0.05\ \mu\mathrm{m} \leqslant a$ with $n(a) \propto a^{-(p=5.5)} \exp\left(-a/a_\mathrm{c} = 0.3\ \mu\mathrm{m}\right)$. The power index p is significantly steeper than that for interstellar dust ($p \sim 3$). Similar results have also been found in some other PPNs and suggest that mechanisms that grind down large particles, such as sputtering, may also have acted when the dust particles formed. The spectral opacity index β is found to be 0.6±0.5 from the 760 μm to 2.6 mm fluxes, which is characterised by the dust in the torus. This low value (<2) indicates the presence of large dust grains in the torus. We discuss two possible dust models for the torus. One has a size distribution function of $1.0\ \mu\mathrm{m} \leqslant a \leqslant a_\mathrm{max} = 5\,000.0\ \mu\mathrm{m}$ with $n(a) \propto a^{-(p=2.5)}$ and the other is $1.0\ \mu\mathrm{m} \leqslant a \leqslant a_\mathrm{max} = 10\,000.0\ \mu\mathrm{m}$ with $n(a) \propto a^{-(p=3.5)}$. The former has β of 0.633, but we are not able to find reasonable geometry parameters to fit the SED in the infrared. The latter has β of 1.12, but reproduces the SED better over a wide wavelength range. With this dust model, the geometric parameters are estimated as follows: the inner and outer radii are 30 AU and 1000 AU and the torus mass is 3.0 $M_\odot$. Given that the torii are generally not found to be rotating, a large fraction of the torus material is likely to be expanding. Assuming an expansion velocity of 15 kms^{-1}, the torus formation time and mass-loss rate are found to be ∼300 yrs and ∼10^{-2} $M_\odot$yr^{-1} respectively.

Key words: Stars: AGB and post-AGB – circumstellar matter – radiative transfer – polarization – individual (IRAS 18276–1431)

1 INTRODUCTION

IRAS 18276–1431 (hereafter I18276), also known as OH 17.7–2.0, is an oxygen-rich proto(pre)-planetary nebula (PPN). This object has been well studied in maser observations over the past three decades since its discovery as a strong OH 1612 MHz source (Bowers 1978). No SiO maser has been detected (Nyman et al. 1998). The intensity of the H$_2$O maser dropped by a factor of a hundred during the period between 1985 and 1990 and is now undetectable, indicating that the mass-loss rate has rapidly decreased to below 10^{-7} $M_\odot$yr^{-1} (Engels 2002). These maser properties

suggest that the central star evolved off the asymptotic giant branch (AGB) phase very recently.

The dust shell of this object has also been the subject of several studies. Sánchez Contreras et al. (2007, hereafter SC07) presented optical *HST/WFPC2* images and infrared K_P, L_P, and M_S images from the Keck II telescope. The images show a striking bipolar appearance with an extension of ∼2 arcsec×3 arcsec. While the extension and the appearance look similar in these shorter wavelength ranges, the mid-infrared images at 8.59 μm, 11.85 μm, and 12.81 μm show an elongated shape along the polar direction with a flux peak towards the central star (Lagadec et al. 2011). SC07

also performed a one-dimensional (1D) double shell model that mainly fits the mid-infrared flux. They found that the observed fluxes between 800 μm and 2.6 mm are roughly proportional to ν^2, where ν is the frequency, indicating the opacity coefficient $Q_\nu \sim 1$. Hence, they concluded that the dust grains with radii $a \gtrsim 400$ μm could explain the flux slope at these wavelengths.

The dust growth in the circumstellar environment is an interesting issue. If the ejected material radially expands at typical expansion velocities of ~ 15 kms^{-1}, the dust particles may only grow a little and retain the properties that were set in the dust formation region. That is to say, particles with sizes up to a few micron should exist. This is confirmed in several previous papers (e.g. Jura & Morris 1985). Bipolar objects such as I18276 are expected to have an optically thick, long-lived dust torus or disc around the central star, which is thought to have formed because of binary interactions (e.g. Morris 1987). In such a thick dusty region, the dust grows in size by mutual collisions. Although the formation of the disc/torus and the dust processes therein have been studied in various object classes, they are still under debate and present some intriguing problems.

In the present work, we investigate the dust properties in I18276's circumstellar dust shell (CDS) by means of two-dimensional (2D) radiative transfer calculations. An approximate solution was obtained by SC07's 1D SED model. However, since I18276 exhibits a striking bipolar lobe, we explore 2D modeling. Furthermore, the spectral slope of the (sub)millimeter flux is often used to detect large grains of a few hundred micron or larger. In our modeling, we encounter difficulties explaining the millimeter flux excess and the fluxes at far-infrared or shorter wavelengths simultaneously with a reasonable mass of the material in the equatorial region. We will revisit the spectral slope issue.

2 DUST SHELL MODELING

We performed 2D radiative transfer modeling of I18276's CDS. Our aim is to investigate the dust properties in the envelope and the equatorial region. An analysis of the arc-like structure and the "search light" feature, which are detected in previous optical and NIR images (SC07), and the formation of bipolarity are beyond the scope of this work. A comprehensive discussion on the morphology can be found in SC07. Our modeling approach is basically similar to our previous work (Murakawa et al. 2010a; Murakawa 2010b). We used NIR polarimetric data obtained with VLT/NACO, these data are particularly useful to estimate the dust sizes. This is complemented by SED data collected from various sources. The results of the HST and Keck images (SC07) and the VISIR image (Lagadec et al. 2011) are weighted less to constrain the parameters in our 2D modeling. In the following subsections, the archival data, model assumptions, and the results for the selected model are presented.

2.1 Observational constraints

Figure 1 shows the SED of I18276, it has a single flux peak at ~ 25 μm and a weak 10 μm absorption feature. In this plot, the interstellar reddening, which is calculated to be
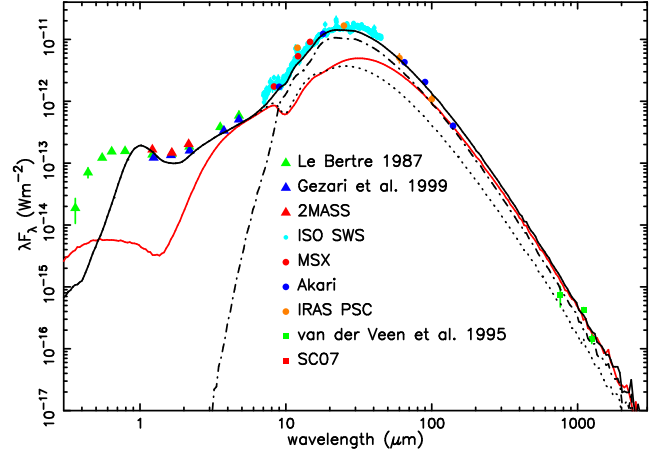

Figure 1. The observed SED of I18276, with the model results over plotted. The solid, dotted, and dashed-dotted curves denote the total flux, the scattered light, and the thermal emission, respectively. The black lines represent the model with the torus and envelope. The red line denotes the model with only the torus. The sources for the photometry are in order of wavelength, from the optical to millimeter: Le Bertre (1987), Catalog of Infrared Observations, Edition 5 (Gezari et al. 1999), 2MASS all-sky catalogue of point sources, Akari/IRC mid-IR all-sky Survey (Ishihara et al. 2010), the calibrated data (the data ID of 10802940) of the ISO Short Wavelength Spectrometer (Kraemer et al. 2002), MSX infrared point source catalogue, IRAS point source catalogue, and SC07. For the data where the error bars are not seen, the uncertainties are smaller than the plot symbols.

1.6($\pm$0.5) mag at V (SC07), is used to correct the measured fluxes for wavelengths shorter than 5 μm.

The upper panels of Fig. 2 present the NIR images, which are collected from the VLT/NACO data archive. The natural seeing was 0.5 arcsec to 0.6 arcsec in the optical during the observations, which is typical for the Paranal site. The H and K_S band data were taken with the Wollaston prism to measure the polarisation. The data were reduced following the same method as before (Murakawa & Izumiura 2012). Standard star data were used to calibrate the surface brightness and the polarisation, and also served to estimate the size of the point spread function (PSF). The measured full widths at half maximum of the beam are 0.1 arcsec, 0.058 arcsec, and 0.063 arcsec in the J, H, and K_S bands, respectively. The PSFs were modeled using one-dimensional Moffat function fitting. The PSF size 2σ and slope β are obtained to be 0.146 arcsec and 1.17 in the J-band, 0.074 arcsec and 1.18 in the H-band, and 0.048 arcsec and 1.03 in the K_S-band. The model images are convolved with the model PSF which allows comparison with the observed images. The intensity images show a striking bipolar appearance and look similar in the J, H, and K_S bands, consistent with previous observations (e.g. SC07). For the H and K_S band images, the polarisation vectors are overlaid. The vectors are aligned perpendicularly to the bipolar axis. The polarisation reaches 50 – 60 % and does not change much between the H and K_S bands. There is no significant difference between the upper, brighter and lower, fainter lobes.

In our modeling, we aim to fit the shape of the SED including the weak 10 μm silicate feature, the constant bipolar appearance and degree of polarisation in the NIR.
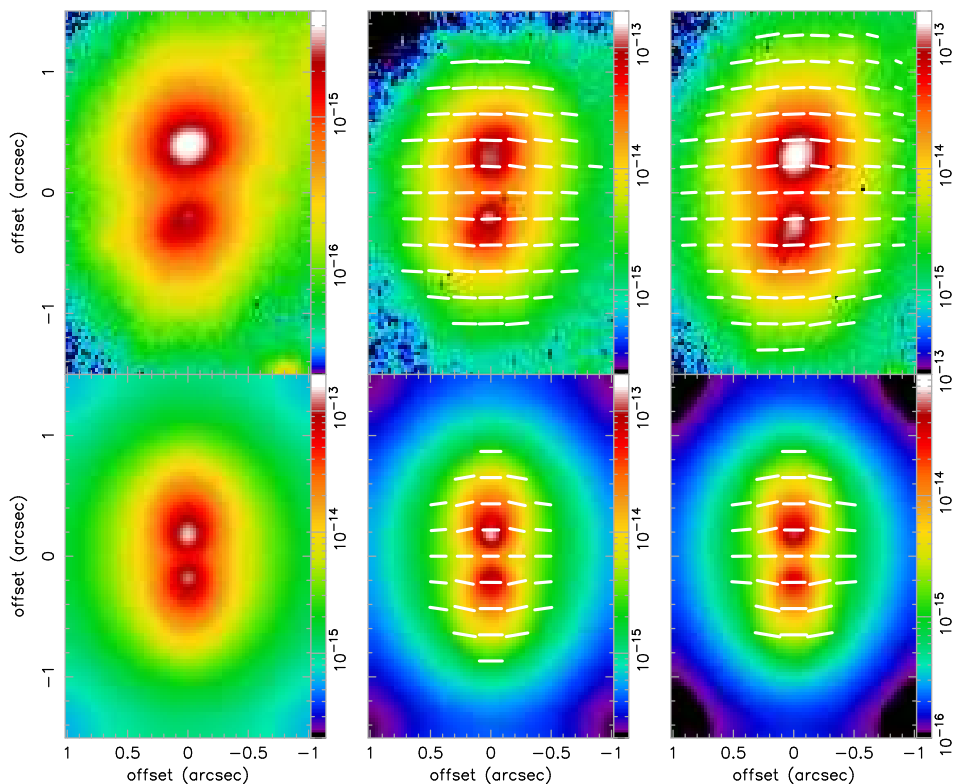
Figure 2. *Left three columns:* J, H, and K_S-band images. Top and bottom panels are from the VLT/NACO archived and our model results, respectively. The color scale bars indicate the surface brightness in $\mathrm{W m^{-2} \mu m^{-1} arcsec^{-2}}$. In the H and K_S-band images, the polarisation vector lines are overlaid. The modelled images are convolved with a one-dimensional Moffat model PSF.

2.2 Model assumptions

The spectral type and the total luminosity of the central star are estimated to be $\sim$K5 or earlier and $\sim 1.5 \times 10^4 \left(D \text{ kpc}/4.6\right)^2$, respectively (Le Bertre et al. 1989). Previous OH maser phase-lag measurements yielded a distance in the range 3.4 to 5.4 kpc (Bowers et al. 1981, 1983). In our model, the central star is assumed to have a blackbody spectrum with 7000 K, which is an intermediate value of the previous estimates of 4000 K to 10 000 K (e.g. Le Bertre et al. 1989). We adopted the distance to be 3 kpc following SC07, yielding a luminosity of 6380 $L_\odot$. We will start with this value, but will eventually use 8500 $L_\odot$ to better fit the SED.

In bipolar PPNs such as I18276, it is expected that the CDS has an optically thick dust torus/disc in the equatorial region and an envelope, which characterises the lobe shape. In our separate paper on the bipolar PPN IRAS 16342–3814, we needed an additional optically thick, geometrically thin disc inside the torus (Murakawa & Izumiura 2012). For I18276, we tried both model geometries, but found that the inner disc is not necessary. The mass density form for I18276 is assumed to be $\rho = \rho_{\text{torus}} + \rho_{\text{lobe}} + \rho_{\text{AGB}}$. We apply a mass density form $\rho_{\text{torus}}(r, z) = \rho_{\text{t}} \left(r/R_{\text{torus}}\right)^{-2} \exp\left(-z^2/2 \left(H_0 r\right)^2\right)$ for the torus, where (r, z) are the two-dimensional cylindrical coordinates, and the torus region is defined as $R_{\text{in}} \leqslant \sqrt{r^2 + z^2} \leqslant R_{\text{torus}}$. We would like to stress that the dust particle motions in the torii of evolved stars are not well known. For example, it is not clear whether they are accreting onto the star, expanding, or rotating in a Keplerian fashion, or not. Hence,

we regard the torus just as a tapered dust structure. For the envelope, we assume a spherical AGB shell in the outer part and a pair of bipolar lobes inside the AGB shell. This is because the mass-loss rate rapidly increases at the very end of the thermal pulsing AGB phase. The lobe is then carved out by the fast wind when the star evolves to the post-AGB phase. The bipolar appearance is mainly characterised by the lobe structure. The mass density forms of the lobe and AGB shell are given by equations (4) and (5) in our I16342 paper, respectively. They are determined by the density coefficient, ρ_{e}, the density ratios ϵ_{in} and ϵ_{rim}, for the inner cavity and the rim of the lobe; the lobe shape, β, the lobe thickness, γ, the lobe size, R_{lobe}, and the outer radius R_{out}. The mass density coefficients, ρ_{t} and ρ_{e}, are determined from the masses of the torus and envelope (i.e. lobe and AGB shell) assuming a gas-to-dust mass ratio of 200. The important parameters are the radii of the inner R_{in} and outer R_{torus} boundaries of the torus, the aspect ratio of the torus height H_0, the masses of the torus M_{torus} and the envelope M_{env}, γ, ϵ_{in}, and ϵ_{rim} are determined in our modeling. The other parameters such as β, R_{lobe}, and R_{out} are set to be fixed values. Figure 3 shows the mass density map of the inner 2000×3000 AU region.

The mineralogy of dust in the CDS is not well known. We therefore simplify the dust model and adopt the optical constants of oxygen deficient silicate (Ossenkopf et al. 1992). We assume different dust sizes for the torus and the envelope. The dust size in the envelope can be constrained with polarimetric data. We assume a KMH-like size distribution function (Kim et al. 1994): $n(a) \propto a^{-p} \exp\left(-a/a_{\text{c}}\right)$
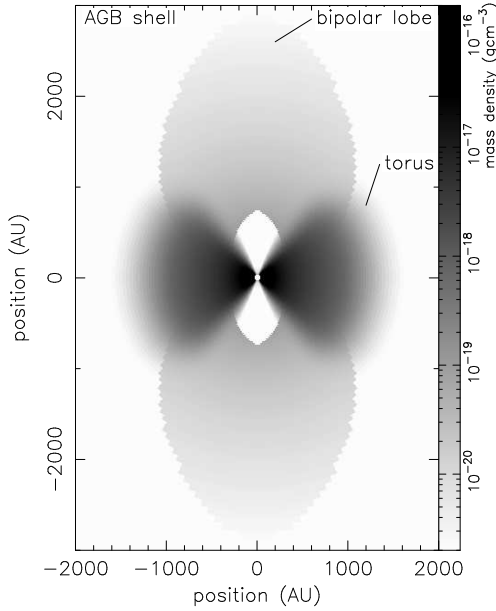
Figure 3. Mass density distribution of the model in a plane cutting through the symmetry axis. The parameters are from the selected model (see Table 1). The AGB shell is not explicitly indicated, because the mass density is lower than 2×10^{-21} gcm^{-3}, but it exists outside the bipolar lobe and torus.

Table 1. Model parameters of I18276's circumstellar dust shell.

parameters	values	comments[1]
	central star	
T_{eff}	7000 K	Le Bertre et al. (1989)
$L_\star$	8500 $L_\odot$	adopted[2]
D	3.0 kpc	SC07
$R_\star$	4.38×10^{13} cm	calculated
	torus	
R_{in}	30 AU	$20-30$
R_{torus}	1000 AU	$700-1500$
H_0	1.0	$0.8-1.2$
M_{torus}	3.0 $M_\odot$	$2.5-4.0$
a_{min}	1.0 μm	adopted
a_{max}	10 000.0 μm	$\gtrsim 1000.0$
$\tau_{5\mu\mathrm{m}}$	52	calculated
	bipolar lobe and AGB shell	
R_{lobe}	3000 AU	adopted[3]
β	1.0	adopted
γ	0.75	$0.7-0.8$
ϵ_{in}	0.01	< 0.1
ϵ_{rim}	10	$10-15$
R_{out}	90 000 AU	adopted
M_{env}	1.2 $M_\odot$	$1.0-1.5$
a_{c}	0.3 μm	$0.3-0.4$

[1] Ranges give the uncertainty of the corresponding model parameters. [2] Based on comparison of the SED. [3] Based on comparison with the intensity image.

with a_{min} of 0.05 μm and note that a steep power index p of 5.5 results in a weak wavelength dependence. Only **the cutoff size,** a_{c}, is a free parameter. The wavelength dependency of the power index p will be discussed in Sect. 3.1.

The dust sizes in the torus can be constrained with the spectral flux slope α in the (sub)millimeter wavelength ranges. With the flux data between 761 μm and 2.6 mm, α is 2.6±0.5, which yields the spectral opacity index β of 0.6±0.5 ($= \alpha - 2$). In principle, this allows us to determine a size distribution function, however, it is not a unique solution. We encounter difficulties in fitting the SED at the shorter wavelengths with the derived dust models. The details of this problem will be discussed in sect. 3.2. Instead of applying a dust model that can be determined using β, we attempted to find one that fits the SED better over a wider wavelength range. Assuming an MRN-like size distribution function (Mathis et al. 1977): $n(a) \propto a^{-3.5}$ with $a_{\mathrm{min}} \leqslant a \leqslant a_{\mathrm{max}}$, a_{max} is determined by the SED fitting. For a_{min}, we adopt 1.0 μm. However, since we do not have enough clues to determine the value precisely, we exclude the a_{min} value from the discussion of the dust properties in the torus in Sect. 3.2.

2.3   Results and comparison with the observations

The aforementioned parameters are estimated by means of radiative transfer calculations using our STSH code (Murakawa et al. 2008a). We first tried several parameter sets to get approximate solutions and to understand the parameter dependence on the model results. Then, a few thousand parameter sets were examined by SED fitting. From this result, a dozen good parameter sets are chosen and their images are evaluated. We finally chose one that explains the observations fairly well. We would like to stress that it is very difficult to find a parameter set that reproduces all aspects of the observations. Because our aim is to investigate the dust properties, our modeling is mostly concerned with explaining the NIR polarisation and the SED over a wide wavelength range. The images in the optical and MIR are not accurately reproduced. The derived parameters are: $R_{\mathrm{in}} = 30$ AU, $R_{\mathrm{torus}} = 1000$ AU, $M_{\mathrm{torus}} = 3.0$ $M_\odot$, $a_{\mathrm{min}} = 1.0$ μm, $a_{\mathrm{max}} = 10\,000.0$ μm, the optical depth in the torus midplane is 52 at 5.0 μm, $M_{\mathrm{env}} = 1.2$ $M_\odot$, and $a_{\mathrm{c}} = 0.3$ μm. The viewing angle measured from the polar axis is 80°. Table 1 lists these parameters and uncertainties. We briefly summarise the selected model results in this section and discuss the effects of dust sizes on the model results in detail in sect. 3.

The SED of the selected model is plotted with black lines in Fig. 1. The aperture sizes used for the photometric and spectroscopic data are different for the various observations; they are 4 arcsec in radius (for 2MASS) or larger. Because the apparent size of the nebulosity is small and most flux is concentrated within ∼1 arcsec, the effect of aperture size on the observed SED is negligible in I18276. In fact, the model flux derived applying a 4 arcsec aperture differs less than 1 % from that applying an infinite aperture from optical to millimetre wavelengths. The model fits the observed SED well apart from the optical. The weak 10 μm feature is due to a filling in of the underlying absorption with strong thermal emission. In fact, the MIR images show a flux peak towards the central star (Lagadec et al. 2011) and

the calculated optical depth becomes high as 41 at 10 μm. The red line denotes the result of the selected model but with only the torus, e.g. $M_{\rm env}$ is simply set to be 0. It approximately indicates the contribution from the torus in the selected model. In the wavelengths shorter than ~ 9 μm and between ~ 9 μm and ~ 200 μm, the scattered light and thermal emission from the envelope, respectively, dominate. The SED of the selected model fits the observations comparably well in the NIR and longer wavelengths. However, a large discrepancy is seen in the optical. In some models with other parameter sets, e.g. $a_{\rm min} = 5$ μm dust for the torus and a shallower power index of the mass density distribution in the envelope, we find that these models can fit the SED in the optical better than the selected model. However, these models provide poorer fits to the images or the MIR fluxes.

The bottom panels in Fig. 2 show the model results. The pair of bipolar lobes and a nearly constant appearance from J to K_S bands are reproduced. The optical and MIR images are also reproduced although they are not presented. The bipolarity is seen in the optical, L_P, and M_S bands. On the other hand, the 11.85 μm image shows a single peak. These results are qualitatively consistent with the observations (SC07 and Lagadec et al. 2011). However the details of the surface brightness structures of the images are not accurately reproduced because the images at these wavelengths are not used to strictly constrain the model parameters.

The polarisation vectors are aligned perpendicular to the bipolar axis in the entire nebulosity. Since a centrosymmetric pattern is seen in the raw images, this alignment is due to the PSF smoothing effect, as is also demonstrated in our I16342 paper (Murakawa & Izumiura 2012). The polarisation in the bipolar lobes reaches 50 – 65 %, which is slightly higher than the observations. If $a_{\rm c} = 0.4$ μm is used, the polarisation becomes 45 – 60 %. We confirm that our estimation of the particle size in the envelope is consistent with that by Gledhill (2005).

We reach an important conclusion with respect to the particle sizes. **In the envelope, the mass fraction of the particles with radius larger than the cutoff size ($a_{\rm c} = 0.3$ μm) is 28 %. This fraction decreases dramatically for larger sizes, e.g. only 1.7 % for $a \geqslant 1.0$ μm. The submicron sized dust dominates in the envelope. On the other hand, the fraction of the particles larger than 400 μm is high as 81 % for the torus. Hence, the particles in the torus are expected to be significantly larger than in the envelope.** In Sect. 3.1, we discuss the effect of the power index, p, on the polarization and provide our interpretation on the derived p of 5.5. In Sect. 3.2, we discuss the determination of the particle sizes using the millimeter flux excess and the problems encountered in our modeling.

3 DUST PROPERTIES

3.1 In the bipolar lobe and the AGB shell

In NIR polarimetric images of bipolar reflection nebulae such as those seen around for example evolved stars, young stellar objects (YSOs), and active galactic nuclei, the polarisation vectors are centro-symmetrically aligned and the degree of linear polarisation reaches $\gtrsim 10$ % in general. This
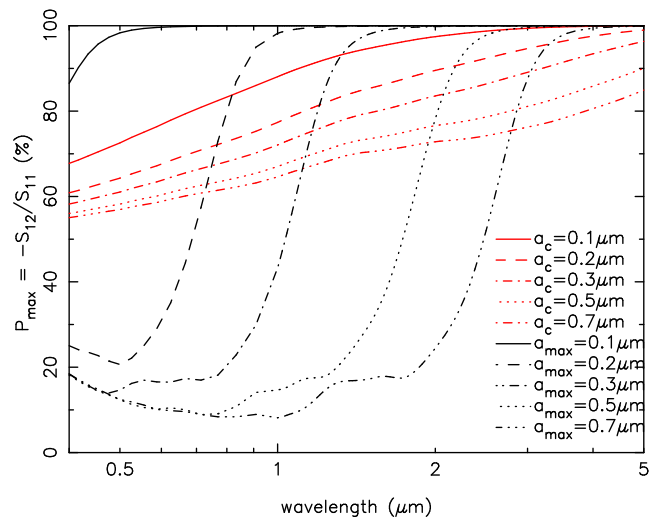
Figure 4. Plot of scattering property. The degree of polarisation is the maximum values of the single scattered light. Red and black lines denote the results of G1 and G2, respectively.

result is explained by single scattering off submicron-sized dust particles. The polarisation is sensitive to the dust size, or to be more precise, the size parameter $x = 2\pi a/\lambda$ for $x \sim 1$. In the case of YSOs, a strong wavelength dependence of the polarisation is seen which can be explained with a size distribution function: $n(a) \propto a^{-3.5}$ (e.g. Hales et al. 2006; Beckford et al. 2008; Murakawa et al. 2008a). This value for the exponent can be readily understood because the dust in the YSO envelope originates from interstellar matter. In contrast, weak wavelength dependencies are found in some evolved stars. The polarisation ranges from 35 to 60 % in the optical to NIR in Frosty Leo (Dougados et al. 1990; Scarrott & Scarrott 1994). Scarrott & Scarrott (1994) found a steeper power index p ranging from 5.2 to 5.5.

We now investigate the effects of the dust sizes and the size distribution function on polarisation. Two models are considered: G1 has 0.05 μm $\leqslant a$ and $n(a) \propto a^{-5.5} \exp(-a/a_{\rm c})$, and G2 has 0.005 μm $\leqslant a \leqslant a_{\rm max}$ μm and $n(a) \propto a^{-3.5}$. Upper limits of the dust size $a_{\rm c}$ or $a_{\rm max}$ of 0.1, 0.2, 0.3, 0.5, and 0.7 μm are examined. Figure 4 presents the resulting polarisation. The degree of polarisation $P_{\rm max}$ is calculated using the ratio of $-S_{12}$ to S_{11} at the scattering angle that maximises the polarisation, where S_{11} and S_{12} are the scattering matrix elements for spherical grains (Bohren & Huffman 1983). These values should be the upper limit of the polarisation expected in the envelope because the scattered light at various scattering angles is integrated in the observed data. In fact, the polarisation values in our model are 50 – 65 % in the H and K_S bands, but the above calculations give 70 – 80 %.

G2 has a strong wavelength dependence in the optical to the NIR, as is observed in YSO envelopes. On the other hand, G1 has a weak dependence in wavelength and dust size. The scattering properties are determined by the relative fractions of small and large dust. The scattering matrix elements S are weighted with $n(a)$ by $< S > = \int S n(a) \, da / \int n(a) \, da$. In G2 the scattering property is dominated by the dust at the maximum sizes. The polarisation varies rapidly around $x \sim 1$, e.g. $\lambda \sim 1$ μm for

$a_{\max} = 0.3$ μm. It is of interest that in fact the polarisations cannot be simultaneously fit in the H and K_S bands if the G2 dust is applied in the envelope in our modeling. For example, whereas the $a_{\max} = 0.4$ μm model reproduces the H band polarization with a value of $P_{\mathrm{H}} \sim 55$ %, the model returns a too high K band polarization of ~ 70 %. The 0.5 μm dust models, instead, reproduce the K band polarization and return $P_{\mathrm{K}} \sim 60$ %, however they result in too low $P_{\mathrm{H}} \sim 27$ %. We see large discrepancies despite a small difference of $\sim$0.1 μm in the $a_{\max}$ values. On the other hand, the G1 model has a larger fraction of small particles ($x < 1$). Thus, the polarisations are higher even at shorter wavelengths, i.e. $\lambda < 1$ μm. In contrast, lower polarisations are obtained at longer wavelengths ($\lambda > 1$ μm) because of the large particles, even though the fractions are low.

It is also useful to note that the polarisations of the G1 models are lower than those of G2 at $\lambda > 3$ μm even with the same upper limit sizes. This is because dust models with the KMH-like size distribution function have particles with sizes exceeding a_{c}. If a steeper power index, e.g. $p = 5.5 > 3.5$, is assumed in the MRN-type dust model, the scattering properties at longer wavelengths ($\lambda \gtrsim 2\pi a_{\max}$) consequently becomes similar to those with a shallower power index. We reach two conclusions. First, in objects that show a weak wavelength dependence in their envelopes such as I18276 and Frosty Leo, a steep power index $p(> 3.5)$ is expected in the size distribution function. Second, if the polarisation is measured over a wider wavelength range such as from the optical to 3 to 5 μm, which is still in the scattering regime in cool dust regions, the size distribution functions are better constrained, e.g. the lower limit and whether the MRN-type or the KMH-type is more favoured.

This brings us to the more general question whether the dust properties depend on the objects under consideration. A NIR polarimetric survey of a dozen of PPNs was presented (Gledhill et al. 2001). Four objects (IRAS 17436+5003, IRAS 19114+0002, IRAS 18095+2704, and IRAS 19500–1709) out of seven for which the nebulosity is spatially resolved, show nearly constant polarisations in the J and K bands. Including three other objects (Frosty Leo, I16342, and I18276), a weak wavelength dependence on polarisation is detected. We thus find similar polarisation behaviour for different morphologies, i.e. spherical, elliptic, and bipolar, while all objects except for IRAS 19500–1709 are oxygen-rich. Differences in morphology are thought to result from the different initial stellar mass, i.e. the higher the mass, the more asymmetry (e.g. Corradi & Schwarz 1995). These observational results suggest that the initial stellar mass and the dust shell morphology do not play important roles in determining the dust size distribution function. The power index of $\sim$3 that is found in the interstellar medium (Mathis et al. 1977) is thought to be the result of dust formation process of mass-losing evolved stars (e.g. Bierman & Harwit 1980).

Dominik, Gail, & Sedlmayr (1989) analysed the dust size spectrum in the dust-driven winds of carbon rich stars. In their models, dust particles form via nucleation at $\lesssim$ 2.0 $R_{\star}$, the size distribution function rapidly approaches the final distribution within $\sim$20 $R_{\star}$. They found that the size distribution functions are proportional to a^{-5} in the case without drift between the gas and dust motions and to a^{-7} in the case with drift. Their results show that large

Table 2. Dust model parameters for the torus

ID	$a_{\max}/p$	β	κ	C_{ext}	M_{torus}	
	μm/		cm^{2}g^{-1}	cm^{2}g^{-1}	$M_{\odot}$	
A	10 000.0/3.5	1.12	1.44	103	3.0	2.11
B	5000.0/2.5	0.633	1.18	4.54	68.1	2.59

The spectral opacity index β and the mass absorptive opacity κ are values at $\lambda = 1.1$ mm. The value of the extinction cross section C_{ext} is for $\lambda = 5.0$ μm. For the torus mass M_{torus}, the values are obtained to keep a constant optical depth at 5.0 μm $\tau = 52$ (left column), i.e. $C_{\mathrm{ext}}M_{\mathrm{torus}}$ is constant, and to fit the flux at $\lambda = 1.1$ mm (right column).

drift velocities steepen the size distribution function because they can break up large particles by sputtering. Woitke (2006) and Höfner & Andersen (2007) pointed out that in oxygen-rich winds, the radiation pressure on the dust is too weak to drive the wind because of low dust opacities. In fact, survey observations of a large number of AGB stars and mass-loss models have shown that expansion velocities are lower in oxygen-rich stars (Groenewegen et al. 1999; Schöier & Olofsson 2001; Olofsson et al. 2002), suggesting lower drift velocities in oxygen-rich stars than the carbon-rich objects. At first glance, this is in the opposite sense to the result that the majority of the objects where steeper power indices are found are oxygen-rich in the aforementioned polarisation survey. Follow up observations of various objects, i.e. C-/O-rich, and various stellar luminosities, mass-loss rates, and evolutionary stages, and further analyses of the dust formation and stellar wind are essential. Although we are not in a position to identify the physical reasons, one may expect that shattering or sputtering works efficiently in the circumstellar environments in objects like I18276.

3.2 In the torus

Measuring the flux excess at submillimeter to millimeter wavelengths provides a simple and powerful method to evaluate whether large dust grains ($\gtrsim$ a few hundred microns) exist in the disc/torus region or not (Beckwith & Sargent 1991; Miyake & Nakagawa 1993; Draine 2006). In fact, numerous previous works have found dust growth particularly in discs around young stars (e.g. Calvet et al. 2002; Testi et al. 2003; Lommen et al. 2007). Some intensive modeling to investigate the effects of the dust growth on the SEDs and images has been done (e.g. D'alessio et al. 2001). In our modeling of I18276, the flux from the torus dominates in the FIR or longer wavelengths (see Fig. 1 and Sect. 2.3). In this result, the dust size in the torus was estimated to fit the SED in a wide wavelength range. In this section, we discuss dust models that fit the flux slope in the submillimeter and millimeter wavelength ranges by applying the aforementioned analysis.

The spectral opacity index cannot be directly determined from observations. Rigorously speaking, it should be derived from the (sub)millimeter flux by solving the radiative transfer problem. In special cases, such as accretion discs (Beckwith & Sargent 1991), approximate solu-
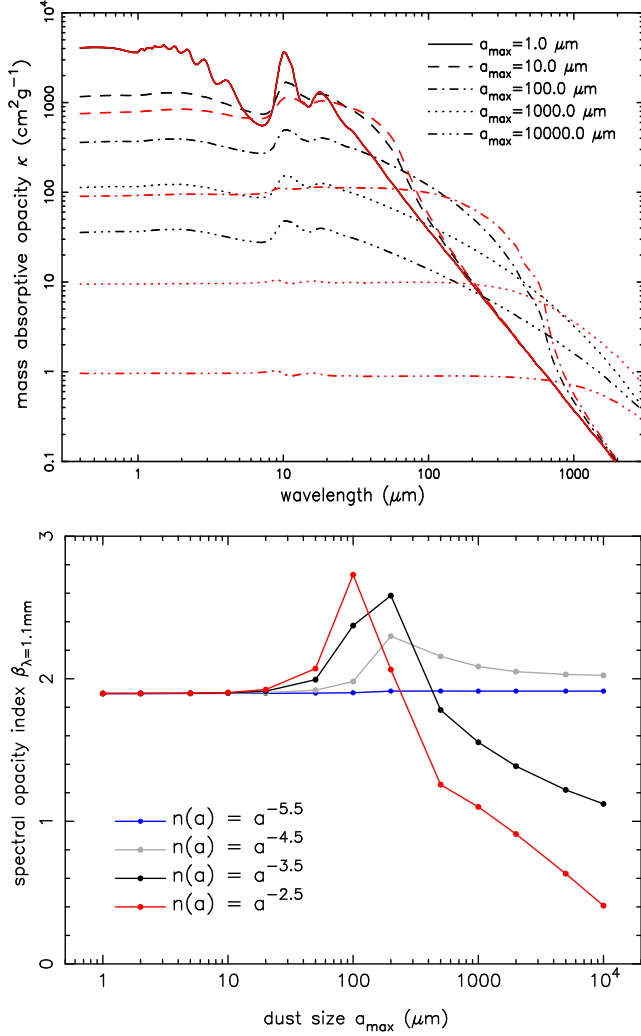
Figure 5. *(top)* mass absorptive opacity $\kappa\,(\lambda)$ and *(bottom)* spectral opacity indices β at $\lambda = 1.1$ mm as function of the maximum size $a_{\max}$. Black and red lines denote dust models with a power index p of 3.5 and 2.5, respectively. The minimum size $a_{\min}$ is set to be 1.0 μm. In the bottom panel, the dust models with a power index of 4.5 (gray) and 5.5 (blue) are also indicated. In the top panel, the plot for the $a_{\max} = 1.0$ μm model is identical to the single sized dust with a radius of 1.0 μm.

tions are given. Here we show a simpler prescription. Let us assume that the flux in that wavelength regime is dominated by emission from the torus and that this emission can be approximated by blackbody radiation with a representative dust temperature, $B_\nu\,(T_{\rm d})$, the flux F_ν is given by $F_\nu \approx M_{\rm torus}\kappa_\nu B_\nu\,(T_{\rm d})\,D^{-2}\zeta^{-1}$, where κ_ν, D, and ζ are the mass absorptive opacity, the distance to the object and the gas-to-dust mass ratio, respectively. If the dust emission at this wavelength range is assumed to be in the Rayleigh-Jeans limit, the blackbody function can be approximated by a power law, $B_\nu\,(T_{\rm d}) \propto \nu^2$. In addition, if the dust opacity has a power-law dependence on frequency, $\kappa_\nu \propto \nu^\beta$, the flux is given by $F_\nu \propto \nu^\alpha$ with $\alpha \equiv d\ln F_\nu/d\ln \nu = \beta + 2$. This can be obtained when the ratio of the optically thick to thin emission, Δ, is neglected in the result derived by Beckwith & Sargent (1991).

    With the observed flux data of I18276 from $\lambda = 761$ μm

to 2.6 mm, β is found to be 0.6$\pm$0.5 where the flux measurement errors are taken into account. Next, we consider β in the dust models. Figure 5 shows the mass absorptive opacity κ and the spectral opacity index β at $\lambda = 1.1$ mm for several spherical dust models, which are calculated using Mie scattering theory. The examined size distribution functions have an MRN-like form with $p = 5.5$, 4.5, 3.5 (G3), and 2.5 (**G4**). The minimum size $a_{\min}$ is set to be 1.0 μm and the maximum sizes that were examined range from 1.0 μm to 10 000 μm. β is constant at ~ 2 for $a_{\max} \leqslant 100.0$ μm, as is known for IS dust. The behaviour of β does not change much for $a_{\min} \lesssim 10$ μm. An anomalous $\beta > 2$ is seen at 100 μm $\leqslant a_{\max} \leqslant 400$ μm. This is due to a sudden drop in the opacity at $x \sim 1$, as seen in the top panel. For $a_{\max} \gtrsim 400$ μm, β monotonically decreases. The behaviour of β depends on the power index p. The absorptive opacity is $\pi a^2 Q\,(a)$, where $Q\,(a)$ is the absorptive coefficient. The fraction of dust opacity to grains with size a or larger, $f\,(a)$, is given by $f\,(a) \gtrsim \left(a_{\max}^{3-p} - a^{3-p}\right) / \left(a_{\max}^{3-p} - a_{\min}^{3-p}\right)$. This should be the lower limit because Q depends on a and is less than unity at smaller a. The larger the p value, the smaller the fraction of large particles. In the dust models with $p = 5.5$ and 4.5, β stays ~ 2 even with large $a_{\max}$ values. In the G3 type, β decreases down to ~ 1. Such a lower limit is reproduced in astronomical silicate particles ($\beta_{\min} \sim 0.85$, Draine 2006). A very low $\beta < 1$ in an oxygen-rich environment implies a lower $p < 3.5$, as seen in G4. We find that a dust model with $a_{\max} = 5000$ μm and $p = 2.5$ has $\beta = 0.633$, which agrees with the observations. We assume the representative temperature of 200 K, which actually varies between 100 K and 700 K in the torus midplane, a distance of 3 kpc, and a gas-to-dust mass ratio of 200. To fit the (sub)millimeter flux, the torus mass should be 2.59 $M_\odot$ for the observed flux of 156 mJy at $\lambda = 1.1$ mm (van der Veen et al. 1995) and the dust opacity at this wavelength of 1.18 cm^{-2}g^{-1}.

    With this dust model, we encounter the serious problem that the NIR flux cannot be reasonably fit. The reason is that the extinction cross section of this dust model is too low in the NIR. It would be easier to understand this using our selected model as reference. The optical depth of the torus is found to be 52 at 5.0 μm. To fit the NIR flux with a dust model other than that used for the selected model, the optical depth of the torus should be kept constant. Namely, $C_{\rm ext}M_{\rm torus}$ should be constant because $\tau_{\rm torus} \propto C_{\rm ext}M_{\rm torus}$, where $C_{\rm ext}$ is the extinction cross section at $\lambda = 5$ μm. Table 2 lists β, κ, $C_{\rm ext}$, and torus masses of two dust models. Whereas $C_{\rm ext}$ of the dust model A (the selected model shown in Figure 1), is high at 103 cm^{2}g^{-1}, that for model B, which fits β, is only 4.54 cm^{2}g^{-1}. The torus mass for model B is required to be unreliably large at 68.1 $M_\odot$. Hence, the β value is more likely close to unity.

    In either estimations ($M_{\rm torus} = 3.0$ $M_\odot$ or 2.59 $M_\odot$), the torus is massive. Even if a binary companion with mass of ~ 1 $M_\odot$ is assumed to exist in I18276's stellar system, it is unlikely that the derived torus has a pure Keplerian rotating motion. Rather a large fraction of the torus material should be radially expanding. A hydrodynamic simulation of a binary interacted outflow model shows a spiral structure in AGB shells even in the models that are classified as bipolar (Mastrodemos & Morris 1999). Similar features are detected in some AGB shells, e.g. NGC 3068 (Mauron & Huggins 2006) and R Scl (Maercker et al. 2012),

although these are optically thin cases. In addition, up to now, a Keplerian rotating motion is detected only for the Red Rectangle (Bujarrabal et al. 2003) while other objects are found to have expanding motions for which the velocity is well studied from observations. Assuming an expansion velocity, V_{exp}, of 15 kms^{-1}, which is an intermediate value of 12 – 17 kms^{-1} (Bowers et al. 1983; Heske et al. 1990, SC07), the torus is formed in ~300 years ($= R_{\text{torus}}/V_{\text{exp}}$). To accumulate a mass of 3.0 $M_{\odot}$, the mass-loss rate should be high as ~10^{-2} $M_{\odot}\text{yr}^{-1}$. Large mass-loss rates lasting a short time at the very end of the AGB phase have been found in some other objects (e.g. Bujarrabal et al. 2001; Sánchez Contreras et al. 2004).

We briefly highlight the problem of dust growth in the torus. In some objects, for which large grains are detected, e.g. the Red Rectangle (Jura et al. 1995; van Winckel et al. 1998) and AFGL 2688 (Bieging & Nguyen 1996; Jura et al. 2000), a long-lived disc is also expected to be present. This is a quite natural expectation because the dust particles have a larger chance to collide and grow in size in a disc than in an expanding outflow, although this is still hypothesised. However, as mentioned above, only for the Red Rectangle a stable rotating disc is detected. The Red Rectangle's Keplerian rotating disc is spatially resolved by CO emission line radio interferometry (Bujarrabal et al. 2005). These authors estimate a disc mass of 0.04 $M_{\odot}$, a radius of 560 AU, and a central mass of ~0.9 $M_{\odot}$. This system is somewhat similar to the solar nebula besides the stellar luminosity. Hence, the dust growth in Red Rectangle can be explained with theories developed for the solar-nebula (e.g. Weidenschilling 1980; Nakagawa et al. 1986). On the other hand, in some objects like I18276 (this work) and IRAS 22036+5306 (Sahai et al. 2006), in which large fractions of large grains are expected in the torus, the torus mass is very high ($\gtrsim$ 1 $M_{\odot}$) and expansion motions are detected. Further studies, in which the dust growth theory should be optimised for the circumstellar environment around evolved stars, are encouraged to better understand such massive large particles in the tori of these objects.

4 CONCLUSION

We modeled the CDS of the oxygen-rich bipolar PPN IRAS 18276–1431 by means of two-dimensional dust radiative transfer calculations. The previously observed SED and NIR polarimetric images were used to constrain the physical parameters. The primary aim of our work was to investigate the dust properties.

The polarisation reaches 50 – 60 % in the bipolar lobes and is almost constant in the H and K_S bands. This weak wavelength dependence and high values can be reproduced by dust models with a steeper power index of 5.5 of the size distribution function than interstellar dust. If the dust in I18276's envelope has conserved its properties since its formation during the AGB phase, mechanisms that break up large grains and increase the fraction of small particles, such as sputtering, may have also acted. Polarization measurements at a large wavelength range for various object classes of C-rich and O-rich, and AGB stars to PNs will provide better constraints of the size distribution functions and will

help our understanding of the dust formation and process in circumstellar environments.

We also investigated the dust properties in the torus. Two candidate dust models were examined. One has a size distribution function of $n(a) \propto a^{-2.5}$ and $a_{\text{max}} = 5\,000$ μm and the spectral opacity index β of 0.633. This model agrees with the observed β of 0.6 from the 760 μm to 2.6 mm fluxes, however, it reproduces too low infrared flux because the opacity is too small. The other dust model has $n(a) \propto a^{-3.5}$ and $a_{\text{max}} = 10\,000$ μm and fits the SED over a wide wavelength range besides the (sub)millimeter opacity slope ($\beta = 1.12$). The torus masses are large for both models; 2.59 $M_{\odot}$ (former) and 3.0 $M_{\odot}$ (latter). In this massive torus, the material is probably radially expanding rather than purely rotating around the central star, as is expected in the previous CO emission line observations. If the expansion velocity of 15 kms^{-1}, which is an intermediate value of the previous estimations, is assumed, the torus has been formed in ~300 yrs with a mass loss rate of ~10^{-2} $M_{\odot}\text{yr}^{-1}$.

REFERENCES

Beckford, A. F., Lucas, P. W., Chrysostomou, A. C., et al. 2008, MNRAS, 384, 907

Beckwith, S. V. W. & Sargent, Anneila I., 1991, ApJ, 381, 250

Bieging, J. H., & Nguyen, Q.-R. 1996, AJ, 112, 706

Bierman, P. & Harwit, M. 1980, ApJ, 241, 105

Bohren, C. F., & Huffmann, D. R., 1983, Absorption and scattering of light by small particles. John Wiley & Sons, New York

Bowers, P. F., 1978, A&AS, 31, 127

Bowers, P. F., Johnston, K. J., & Spencer J. H., 1981, Nature, 291, 382

Bowers, P. F., Johnston, K. J., & Spencer J. H., 1983, ApJ, 274, 733

Bujarrabal, V., Castro-Carrizo, A., Alcolea, J., & Sánchez Contreras, C. 2001, A&A, 377, 868

Bujarrabal, V., Neri, R., Alcolea, J., & Kahane, C. 2003, A&A, 409, 573

Bujarrabal, V., Castro-Carrizo, A., Alcolea, J., & Neri, R. 2005, A&A, 441, 1031

Calvet, N., D'Alessio, P., Hartmann, L. et al. 2002, ApJ, 568, 1008

Corradi, R. L. M. & Schwarz, H. E. 1995, A&A, 293, 871

D'alessio, P., Calvet, N., & Hartmann, L. 2001, ApJ, 553, 321

Dominik, C., Gail, H.-P., & Sedlmayr, E. 1989, A&A, 223, 227

Dougados, C., Rouan, D., Lacombe, F., Tiphene, D., & Forveille, T. 1990, A&A, 227, 437

Draine, B. T. 2006, ApJ, 636, 1114

Engels, D., 2002, A&A, 388, 252

Gezari, D. Y., Pitts, P. S., & Schmitz, M. 1999, yCat., 2225, 0

Gledhill, T. M., Chrysostomou, A., Hough, J. H., & Yates, J. A. 2001, MNRAS, 322, 321

Gledhill, T. M., 2005, MNRAS, 356, 883

Groenewegen, M. A. T., Baas, F., Blommaert, J. A. D. L., Stehle, R., Josselin, E., & Tilanus, R. P. J. 1999, A&AS, 140, 197

Hales, A. S., Gledhill, T. M., Barlow, M. J., et al. 2006, MNRAS, 365, 1348

Heske, A., Forveille, T., Omont, A., van der Veen, W. E. C. J., & Habing, H. J. 1990, A&A, 239, 173

Höfner, S. & Andersen, A. C. 2007, A&A, 465, L39

Hrivnak, B. J., Kwok, S., Volk, K. M. 1989, ApJ, 346, 265

Ishihara, D., Onaka, T., Kataza, H., et al. 2010, A&A, 514, A1

Jura, M., & Morris, M. 1985, ApJ, 292, 487

Jura, M., Balm, S. P., & Kahane, C. 1995, ApJ, 453, 721

Jura, M., Turner, J. L., Van Dyk, S., & Knapp, G. R. 2000, ApJ, 528, L105

Kim, S.-H., Martin, P. G., & Hendry, P. D. 1994, ApJ, 422, 164

Kraemer, K. E., Sloan, G. C., Price, S. D., Walker, H. J. 2002, ApJS, 140, 389

Lagadec, E., Verhoelst, T., Mékarnia, D., et al. 2011, MN-RAS, 417, 32

Le Bertre, T. 1987, A&A, 180, 160

Le Bertre, T., Epchtein, N., Gouiffes, C., Heydari-Mayaleri, M., Perrier, C., 1989, A&A, 225, 417

Lommen, D., Wright, C. M., Maddison, S. T., et al. 2007, A&A, 462, 211

Maercker, M., Mohamed, S., Vlemmings, W. H. T. et al. 2012, Nature, 490, 232

Mastrodemos, N. & Morris, M. 1999, ApJ, 523, 357

Mathis, J. S., Rumple, W., & Nordsick, K. H. 1977, ApJ, 217, 425

Mauron, N. & Huggins, P. J. 2006, A&A, 452, 257

Miyake, K. & Nakagawa, Y. 1993, Icarus, 106, 20

Morris, M. 1987, PASP, 99, 1115

Murakawa, K., Preibisch, T., Stefan, K., & Weigelt, G., 2008a, A&A, 489, 195

Murakawa, K., Ohnaka, K., Driebe, T., Hofmann, K.-H., Oya, S., Schertl, D., & Weigelt, G., 2008b, A&A, 489, 195

Murakawa, K., Ueta, T., & Meixner, M., 2010a, A&A, 510, A30

Murakawa, K., 2010b, A&A, 522, A46

Murakawa, K. & Izumiura, H. 2012, A&A, 544, A5

Nakagawa, Y., Sekiya, M. & Hayashi, C. 1986, Icarus, 67, 375

Nyman, L. A., Hall, P. J., Olofsson, H., 1998, A&AS, 127, 185

Olofsson, H., González Delgado, D., Kerschbaum, F., & Schöier, F. L. 2002, A&A, 391, 1053

Ossenkopf, V., Henning, Th., & Mathis, J. S. 1992, A&A, 261, 567

Sahai, R., Young, K., Patel, N. A., Sánchez Contreras, C., & Morris, M. 2006, ApJ, 653, 1241

Sánchez Contreras, C., Bujarrabal, V., Castro-Carrizo, A., Alcolea, J., & Sargent, A. 2004, ApJ, 617, 1142

Sánchez Contreras, C., Le Mignant, D., Sahai, R., Gil de Paz, A., & Morris, M., 2007, ApJ, 656, 1150

Scarrott, S. M., & Scarrott, R. M. J. 1994, MNRAS, 268, 615

Schöier, F. L. & Olofsson, H. 2001, A&A, 368, 969

Szymczak, M., & Gérard, E., 2005, A&A, 433, L29

Testi, L., Natta, A., Shepherd, D. S., & Wilner, D. J. 2003, A&A, 403, 323

van der Veen, W. E. C. J., Omont, A., Habing, H. J., Matthews, H. E. 1995, A&A, 295, 445

van Winckel, H., Waelkens, C., Waters, L. B. F. M., et al. 1998, A&A, 336, L17

Weidenschilling, S. J. 1980, Icarus, 44, 172

Woitke, P. 2006, A&A, 452, 537